UC San Diego

UC San Diego Electronic Theses and Dissertations

Title
Sparse Stress Structures from Optimal Geometric Measures

Permalink
https://escholarship.org/uc/item/7rd4n81q

Author
Rowe, Dylan

Publication Date
2023

Peer reviewed|Thesis/dissertation

UNIVERSITY OF CALIFORNIA SAN DIEGO

Sparse Stress Structures from Optimal Geometric Measures

A thesis submitted in partial satisfaction of the
requirements for the degree Master of Science

in

Computer Science and Engineering

by

Dylan Rowe

Committee in charge:

Professor Albert Chern, Chair
Professor Chung-Kuan Cheng
Professor Tzu-Mao Li

2023

The thesis of Dylan Rowe is approved, and it is acceptable in quality and form for publication on microfilm and electronically.

University of California San Diego

2023

TABLE OF CONTENTS

LIST OF FIGURES

LIST OF TABLES

ACKNOWLEDGEMENTS

I would like to acknowledge Professor Albert Chern for his support as the chair of my committee. His patience and generosity are manifold, and I'm lucky to have him as a chair of my committee, let alone a mentor.

ABSTRACT OF THE THESIS

Sparse Stress Structures from Optimal Geometric Measures

by

Dylan Rowe

Master of Science in Computer Science and Engineering

University of California San Diego, 2023

Professor Albert Chern, Chair

The minimal stress reconstruction problem asks for a sparse structure supporting an input force distribution while obeying obstacle constraints. In geometric measure theoretic terms, this corresponds to finding a *varifold* satisfying certain physical constraints on its local and global structure. This thesis describes a method which realises such varifolds by representing them as stress matrices which are the optima of an almost-convex optimization problem over a compact domain. This method is able to successfully generate sparse structures with rich internal structure that support a wide variety of force distributions and obstacles.

Chapter 1

Introduction

Geometric measure theory uses *varifolds* as an abstraction for spaces which act like manifolds with branching submanifolds and nonmanifolds. This thesis aims to explore computational applications of these generalized versions of manifolds, motivated by problems in graphics. In Chapter 2, a reprint of a paper submitted for publication to SIGGRAPH Asia, varifolds are realized as non-oriented curves with branching points over $\mathbb{R}^2$ that balance a set of given forces, with potential applications in topology optimization, tensegrity, biology, and even theoretical computer science. Chapter 3 contains a few supplementary experiments, which further delve into the properties and extensions of the algorithm in Chapter 2.

Geometric measure theory often employs the language of topology and differential geometry, and our exploration also uses the language of continuum mechanics to represent varifolds. The rest of this chapter is therefore dedicated to a brief and informal introduction to manifolds, varifolds, and stress tensors, which are useful preliminaries for the content in Chapter 2.

1.1   Manifolds

A manifold is a space that "locally looks like $\mathbb{R}^n$". Slightly more formally, an *n-manifold* is a topological space such that any point has an open neighborhood homeomorphic to $\mathbb{R}^n$. An *n-manifold-with-boundary* is the same definition, but a point may also have a neighbor-
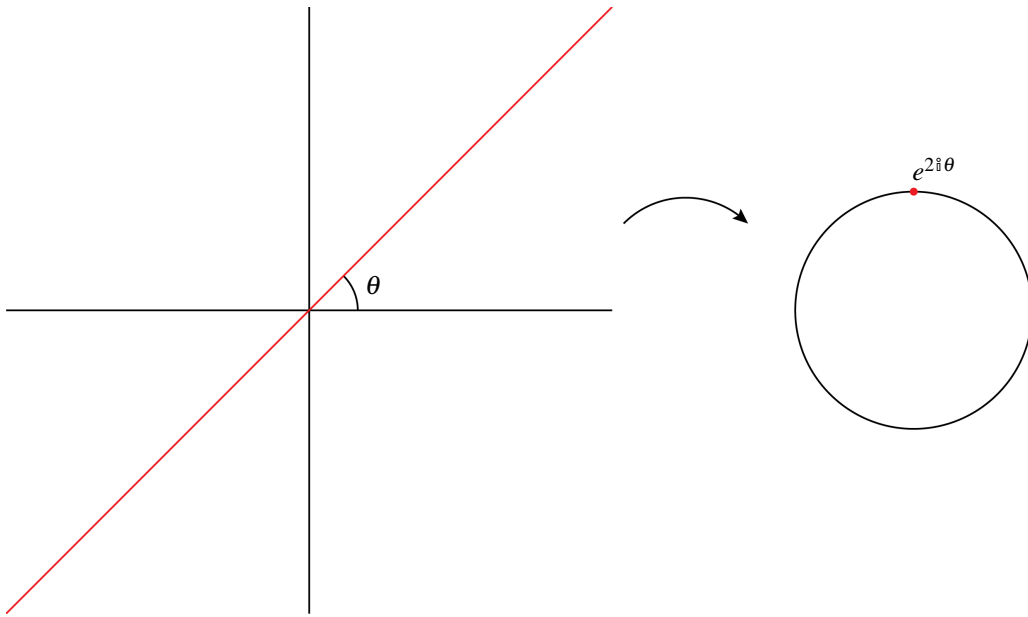
Figure 1.1. $\mathbf{G}(1,\mathbb{R}^2)$ is homeomorphic to the circle by the map taking a line at angle θ to a point at $e^{2\hat{\imath}\theta} \in \mathbb{S}^1 \subset \mathbb{C}$.

hood homeomorphic to the halfplane $\mathbb{R}^n_{x_0 \geq 0}$; points satisfying the second condition are called "boundary points". Boundary points locally look like an "edge" of the manifold-with-boundary.

1.2 Grassmannian Manifold

The Grassmannian manifold, denoted $\mathbf{G}(k,\mathbb{R}^n)$, is the space where each point is a k-dimensional subspace of $\mathbb{R}^n$. One family of notable examples is $\mathbf{G}(1,\mathbb{R}^n)$, each member of which is homeomorphic to $\mathbb{R}\mathrm{P}^{n-1}$. Some of the simplest instantiations of this family are $\mathbf{G}(1,2)$, which is homeomorphic to the circle $\mathbb{S}^1$ (the set of all lines through the origin in $\mathbb{R}^2$ forms a topological circle from angles 0 to π), and $\mathbf{G}(1,\mathbb{R}^3)$, which is homeomorphic to $\mathbb{R}\mathrm{P}^2$. In general, $\mathbf{G}(k,\mathbb{R}^n)$ is a $k(n-k)$ manifold; a proof of this can be found in, for example, [16].

1.3 Varifolds

A varifold is a generalization of a manifold which arises in geometric measure theory. A *m-varifold* over an "ambient space" Ω is simply a (Radon) measure over $\Omega \times \mathbf{G}(m,\mathbb{R}^n)$. It is useful to imagine that a delta measure over such a product space acts like a (non-orientable and possibly singular) k-manifold, where the projection to the Grassmanian part at each point in the support is analogous to the tangent space of a (differentiable) manifold. In the paper

2

reprinted in Chapter 2, our 1-varifold has ambient space $\Omega = \mathbb{R}^2$, and a "delta varifold" under these conditions is simply a planar graph. For a visualization of our varifold over the plane, see Fig. 2.3.

1.4 Stress Tensors

A (Cauchy) stress tensor σ is an element of $\Gamma(\bigwedge^{n-1} T^*M \otimes T^*M)$, where the first component can be considered an "infinitesimal oriented $n-1$-plane" in the base manifold M, and the second component can be considered a traction force assigned to that $n-1$-plane. The Cauchy stress tensor describes the traction force on a given plane in a material body.

When the stress tensor is singular, there is no stress in the singular directions. The first eigenvalue of the stress tensor describes tension (negative) or compression (positive), since inserting the $n-1$ plane with normal equal to that eigenvalue gives a traction force that either pulls or pushes (respectively) in the same direction. The Cauchy stress tensor in a material in equilibrium will always be symmetric, as otherwise there would be torque on an infinitesimal element of the material.

Another useful fact is that stress tensors can also be considered as the type $\Gamma(TM \otimes TM \otimes \bigwedge^n T^*M)$, where the isomorphism to the previous formulation is given by converting one tangent space to a cotangent space using a metric on M, and then inserting the other tangent space into $\bigwedge^n T^*M$. It can be shown that the two tangent spaces factors are interchangeable, and thus in Chapter 2 the stress tensor is sometimes written as an element of $\Gamma(TM \otimes_{\text{sym}} TM \otimes \bigwedge^n T^*M)$.

One important identity is that contracting with the differential operator along one index gives the equilibrium force distribution of the material with that stress tensor, *i.e.* for a force distribution described in coordinates by $\mathbf{f} = \sum f_j e_j$,

$$(\partial_i \sigma^{ij}) e_j dA = f_j e_j dA \tag{1.1}$$

or, more succinctly,

$$\text{div}\,\sigma = \mathbf{f} \tag{1.2}$$

where $\mathbf{f}$ is the equilibrium force distribution on the body. This fact can be interpreted as saying that the sum of all outgoing forces on an infinitesimal element should be zero everywhere except at the points with nonzero force distribution, where this sum is equivalent to the force distribution at that point. In Chapter 2, this fact is exploited to find materials with stress distributions which balance a given force distribution.

Chapter 2

Sparse Stress Structures from Optimal Geometric Measures
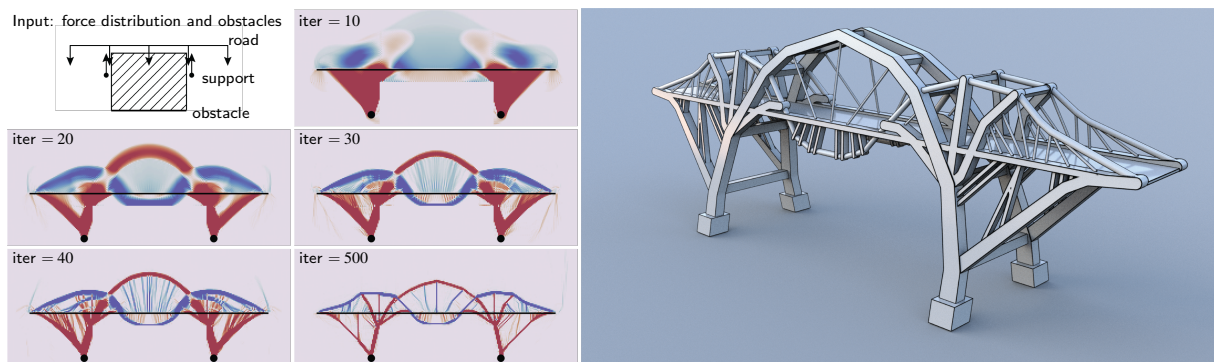
Figure 2.1. A bridge with a hybrid suspension–tied-arch support structure designed by a simple geometric optimization algorithm derived from geometric measure theory. Given a user prescribed force distribution to support and obstacles to avoid (top left), the algorithm efficiently finds a sparse geometric measure (a *varifold*) representing a sparse stress distribution balancing the force (left), performing at 25 iterations per second without GPU acceleration. The blue and red colors visualize the sign of the trace of the stress tensor, indicating tension and compression respectively. We build a 3D model of the bridge using the optimization result as blueprint (right).

2.1 Introduction

Designing the geometry for a sparse support structure is an important task in topology optimization and structural design, yet it remains a computational challenging problem. Typically, the problem is formulated as a large-scale parameter optimization problem over an elastostatic solver or as a combinatorial problem [21]. In this paper, we approach the subject matter by considering a geometric graph optimization problem:

Figure 2.2. Given loading forces $\mathbf{f}_i$'s at some nodes $\mathbf{p}_i$'s in the presence of obstacles, find a minimal graph of struts and cables that form a structure capable of supporting the forces while avoiding obstacles.

> *Find a minimal network of curves connecting a given set of ends while avoiding a given set of obstacles, so that it represents a minimal supporting structure for a given set of loading forces given at the ends.*
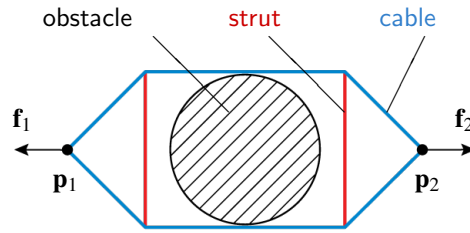
We refer to this problem as the *minimal stress reconstruction problem*. Using geometric measure theory, we demonstrate that this problem can be formulated as a simple and almost-convex continuous optimization problem. We also show that approximate solutions to this problem exhibit intricate emergent geometric structures and patterns such as branches, trusses, and arches (Fig. 2.1). Despite the simplicity of the mathematical model, the phenomenological richness of its results suggests numerous potential applications in topology optimization, architecture and tensegrity structure design, as well as theoretical connections to the study of branched optimal transport [29, 2, 19] and cytoskeletal networks [25, 12].

This paper focuses on the minimal stress reconstruction problem in the plane with arbitrary obstacles and weights. The optimization algorithm is a simple iterative scheme involving only fast Fourier transforms and local calculations.

2.2 Related Work

Topology Optimization

Topology optimization aims to find topology and shape for a structure using bounded material which also minimizes a physical energy (typically stress-strain energy). The diverse range of methods used for topology optimization constitute a wide and deep body of literature

[21], [22], [7], and include greedy heuristic methods, levelset optimization methods, and genetic algorithms [20]. While topology optimization methods often enforce the divergence constraint mentioned here, they tend to manage the material volume using explicit constraints on the total density. Our method instead directly minimizes the support of our stress tensor, and thus describes a different class of optimization problems. Compared to traditional topology optimization, our model is simpler and depends on fewer parameters, and thus we believe our method could be applied as a lightweight preprocessing step for these methods, which are often bottlenecked by a stress simulation step.

Tensegrity

Tensegrity, which is short for "tensile integrity" [9], is a mechanical paradigm characterized by cables and struts supporting a structure in equilibrium. It has previously been posed as a mixed integer program [8], and also has relaxations involving semidefinite programs [23, 24, 28], with rich connections to the geometric realization of graphs. Tensegrity also has applications to architecture [10], cell biology [25, 12], robotics [18, 11], and space structures [26]. Our algorithm's output can be interpreted as a tensegrity structure whose topology has been optimized using an Eulerian method.

Varifold Methods

Varifolds are a generalization of manifolds from geometric measure theory which have appeared in some computer scientific contexts in the past. [4] uses "discrete varifolds" to approximate the mean curvature of input geometry. [5] employ varifolds to handle registration for potentially nonorientable shapes. Our method uses a varifold formulation to find potentially nonorientable and nonmanifold surfaces matching a certain force distribution.

Computational Geometric Measure Theory

A recent method uses geometric measure theoretic formulations to find area-minimizing surfaces over 3-dimensional domains [27]; extensions to this work used deep learning to increase

resolution and generalize the method to arbitrary shapes with boundary [17]. Critically, unlike these methods, our method is able to handle nonorientable submanifolds with branch points.

2.3 Theory

Given $V_0 = \{\mathbf{p}_0, \dots \mathbf{p}_m\} \subset \mathbb{R}^2$ and $\mathbf{f}_0, \dots \mathbf{f}_m \in \mathbb{R}^2$, the minimal stress reconstruction problem asks for an $\mathbb{R}^2$-embedded undirected graph (V, E), $V \supset V_0$, and tensions $(\lambda_{ij})_{ij \in E} \in \mathbb{R}$ such that for every vertex $i \in V$

$$\sum_{j \in \mathrm{Nbr(i)}} \lambda_{ij} \frac{\mathbf{p}_j - \mathbf{p}_i}{|\mathbf{p}_j - \mathbf{p}_i|} + \mathbf{f}_i = 0. \tag{2.1}$$

Here, $\mathbf{f}_i$ is considered to be 0 on $V \setminus V_0$. This is the condition that the graph forms a structure in equilibrium which exerts the prescribed forces on vertices in V_0. We also seek to find the graph with minimal edge length among all graphs satisfying these properties, where edge length is denoted $\ell_{ij} = |\mathbf{p}_i - \mathbf{p}_j|$:

$$\text{minimize} \sum_{ij \in E} \ell_{ij} \quad \text{subject to (2.1).} \tag{2.2}$$

In the language of geometric measure theory, any planar weighted graph is a 1-dimensional *weighted varifold* in the plane, which is a signed measure over the Grassmannian bundle $\mathbb{R}^2 \times \mathbf{G}(1, \mathbb{R}^2)$. Here, the Grassmannian manifold $\mathbf{G}(1, \mathbb{R}^2)$ is the collection of 1-dimensional subspaces in $\mathbb{R}^2$, which is the space of all unsigned planar directions. Note that $\mathbf{G}(1, \mathbb{R}^2) \simeq \mathbb{S}^1$. We denote the measure (*i.e.* weighted varifold) corresponding to our weighted graph $\rho \in \mathcal{M}(\mathbb{R}^2 \times \mathbf{G}(1, \mathbb{R}^2))$. The total length of the edges in the planar embedding of this graph is given by the volume of the support of this measure, *i.e.*,

$$\sum_{ij \in E} \ell_{ij} = \int_{\mathbb{R}^2 \times \mathbf{G}(1, \mathbb{R}^2)} \mathrm{supp}(\rho). \tag{2.3}$$
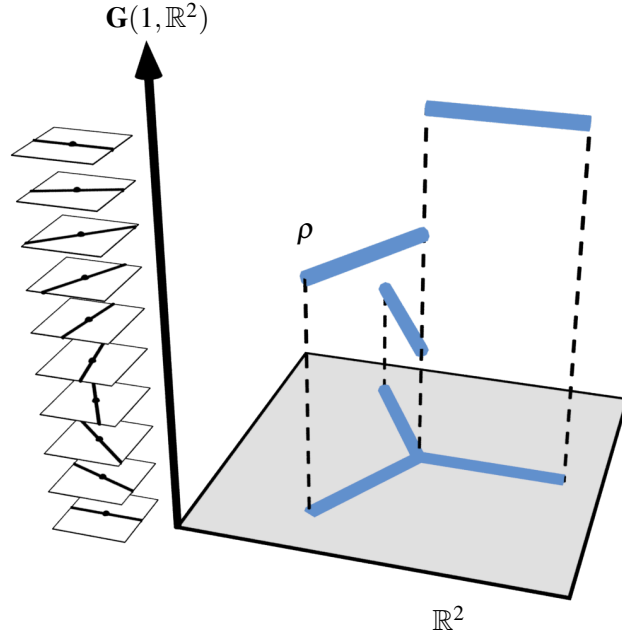
8

Figure 2.3. A varifold representing a planar graph is a distribution over $\mathbb{R}^2 \times \mathbf{G}(1,\mathbb{R}^2)$

The problem can now be viewed as searching a measure over the nonlinear manifold $\mathbb{R}^2 \times \mathbf{G}(1,\mathbb{R}^2)$. Next, we work with the varifold linear algebraically by invoking the *Veronese map* $\mathscr{V}: \mathbf{G}(1,\mathbb{R}^2) \hookrightarrow \mathbb{R}^{2\times 2}_{\text{Sym}} = \mathbb{R}^2 \otimes_{\text{sym}} \mathbb{R}^2$, which takes an element in $\mathbf{G}(1,\mathbb{R}^2)$ represented by unit tangent vector $\mathbf{e}_\theta = (\cos\theta, \sin\theta)^\intercal \in \mathbb{R}^2$ to the symmetric matrix $\mathbf{e}_\theta \mathbf{e}_\theta^\intercal \in \mathbb{R}^{2\times 2}_{\text{Sym}}$. This Veronese map induces a linear map from weighted varifolds to symmetric-matrix-valued measures over the plane:

$$\mathscr{V}_\#: \mathscr{M}(\mathbb{R}^2 \times \mathbf{G}(1,\mathbb{R}^2)) \to \Gamma(T\mathbb{R}^2 \otimes_{\text{sym}} T\mathbb{R}^2 \otimes \textstyle\bigwedge^2 T^*\mathbb{R}^2), \tag{2.4}$$

which takes each basis element $\delta_{(\mathbf{x},\theta)} \in \mathscr{M}(\mathbb{R}^2 \times \mathbf{G}(1,\mathbb{R}^2))$ to $\mathscr{V}_\# \delta_{(\mathbf{x},\theta)} := \mathbf{e}_\theta \mathbf{e}_\theta^\intercal \delta_{\mathbf{x}}$. Physically, $\mathscr{V}_\# \rho$ represents the stress distribution of the weighted varifold ρ. On the space of symmetric matrix measures, we have the divergence operator

$$\text{div}: \Gamma(T\mathbb{R}^2 \otimes_{\text{sym}} T\mathbb{R}^2 \otimes \textstyle\bigwedge^2 T^*\mathbb{R}^2) \to \Gamma(T\mathbb{R}^2 \otimes \textstyle\bigwedge^2 T^*\mathbb{R}^2) \tag{2.5a}$$

given by contracting the differential operator and the tensor along one index:

$$\mathrm{div}\left(\sigma^{ij}\mathbf{e}_i\mathbf{e}_j dA\right) := (\partial_i \sigma^{ij})\mathbf{e}_j dA. \tag{2.5b}$$

The divergence of the symmetric tensor represents the net traction force from the stress. In other words, the stress equilibrium condition

$$\mathrm{div}\,\mathcal{V}_{\#}\rho = \mathbf{f} \tag{2.6}$$

is the varifold equivalent of (2.1). Here, $\mathbf{f} := \sum_{i=0}^m \mathbf{f}_i \delta_{\mathbf{p}_i} \in \Gamma(T\mathbb{R}^2 \otimes \wedge^2 T^*\mathbb{R}^2)$ represents the force distribution as a vector-valued measure. Using the above representation, we find (2.2) equivalent to the optimization problem

$$\underset{\rho \in \mathcal{M}(\mathbb{R}^2 \times \mathbf{G}(1,\mathbb{R}^2))}{\mathrm{minimize}} \int_{\mathbb{R}^2 \times \mathbf{G}(1,\mathbb{R}^2)} \mathrm{supp}(\rho)$$
$$\text{subject to } \mathrm{div}(\mathcal{V}_{\#}\rho) = \mathbf{f}. \tag{2.7}$$

We recognize this as an instance of the *sparse basis pursuit* problem, which aims to find a sparse linear combination of *atoms* in a *dictionary* which satisfy underdetermined linear constraints. Here, the atom set consists of the point measures $\pm\delta_{(\mathbf{x},\theta)} \in \mathcal{M}(\mathbb{R}^2 \times \mathbf{G}(1,\mathbb{R}^2))$, and the objective on the support of our measure encourages sparsity with respect to this basis.

By performing a change of variables $\sigma = \mathcal{V}_{\#}\rho$ via the linear map (2.4), Problem (2.7) is equivalent to finding a symmetric stress tensor field $\sigma \in \Gamma(T\mathbb{R}^2 \otimes_{\mathrm{sym}} T\mathbb{R}^2 \otimes \wedge^2 T^*\mathbb{R})$ satisfying $\mathrm{div}\,\sigma = \mathbf{f}$ which uses a sparse combination of atoms $\pm\mathcal{V}_{\#}\delta_{(\mathbf{x},\theta)}$.

In compressive sensing, a standard approach converts such problems to norm minimization subject to linear constraints. Namely, define a linearly homogeneous function[1] (referred to as a "norm") $\|\cdot\|$ whose unit ball has sharp corners containing the atom set (Fig. 2.4). Under

---

[1] On a real vector space V, a linear homogeneous function $\|\cdot\| \colon V \to \mathbb{R}_{\geq 0}$ satisfies $\|\lambda\vec{v}\| = |\lambda|\|\vec{v}\|$ for all $\vec{v} \in V$ and $\lambda \in \mathbb{R}$. That is, it is a norm except that it does not need to satisfy the triangle inequality.
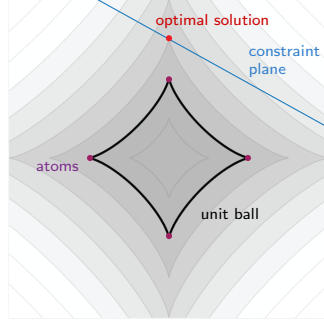
Figure 2.4. When the unit ball has sharp corners containing the atom set, constrained norm minimization leads to sparse solutions.

linear-constrained norm minimization, these sharp corners generally lead to sparse solutions, as it is likely that the constraint affine plane will be tangential to the norm levelsets at these corners, which consist of few atoms.

One can design such a unit ball by, for example, taking the convex hull of the atom set; this choice corresponds to the L^1 convex relaxation. Even sparser results can be obtained by using sharper star shapes, mildly sacrificing convexity. Our method adopts the (nonconvex) (p,q)-spectral norm with $0 < p < 1, 0 < q < 1$. With the singular value decomposition $\sigma = (U\Sigma V^\mathsf{T})\, dA$, the spectral p-norm[2] is the p-norm applied to the singular values ($|\sigma|_p := (\operatorname{tr}\Sigma^p)^{\frac{1}{p}}$). Then, our (p,q)-spectral norm is

$$\|\sigma\|_{p,q} := \left(\int_{\mathbb{R}^2} |\sigma|_p^q \, dA \right)^{\frac{1}{q}}. \tag{2.8}$$

Finally, our optimization problem takes the form

$$\underset{\sigma \in \Gamma(\otimes^2_{\mathrm{sym}} T\mathbb{R}^2 \otimes \wedge^2 T^*\mathbb{R})}{\operatorname{minimize}} \|\sigma\|_{p,q} \tag{2.9}$$

$$\text{subject to } \operatorname{div}\sigma = \mathbf{f}.$$

---

[2] $|\sigma|_p$ is also known as the Schatten p-norm.

2.3.1 Divergence and the Killing Operator

Here, we analyze the divergence operator (2.5) for symmetric tensor measures, as it is the linear operator central to our optimization problem (2.9). The divergence operator is a linear operator from the space of symmetric tensor measures to the space vector measures. Its adjoint is minus the *Killing operator* $\mathscr{K}$ [1, 6]

$$\mathscr{K} : \Gamma(T^*\mathbb{R}^2) \to \Gamma(T^*\mathbb{R}^2 \otimes_{\mathrm{sym}} T^*\mathbb{R}^2), \tag{2.10a}$$

$$\mathscr{K}(\alpha_i dx^i) := (\partial_i \alpha_j + \partial_j \alpha_i) dx^i dx^j, \tag{2.10b}$$

completing the canonical duality diagram:

$$\begin{array}{ccc}
\Gamma(T\mathbb{R}^2 \otimes_{\mathrm{sym}} T\mathbb{R}^2 \otimes \wedge^2 T^*\mathbb{R}^2) & \xrightarrow{\mathrm{div}} & \Gamma(T\mathbb{R}^2 \otimes \wedge^2 T^*\mathbb{R}^2) \\
\text{\scriptsize dual} \Big\vdots & & \Big\vdots \text{\scriptsize dual} \\
\Gamma(T^*\mathbb{R}^2 \otimes_{\mathrm{sym}} T^*\mathbb{R}^2) & \xleftarrow{\mathrm{div}^* = -\mathscr{K}} & \Gamma(T^*\mathbb{R}^2).
\end{array} \tag{2.11}$$

The dual pairing between an element $\sigma \in \Gamma(T\mathbb{R}^2 \otimes_{\mathrm{sym}} T\mathbb{R}^2 \otimes \wedge^2 T^*\mathbb{R}^2)$ and an element $\tau \in \Gamma(T^*\mathbb{R}^2 \otimes_{\mathrm{sym}} T^*\mathbb{R}^2)$ is given by $1/2$ of the integrated Frobenius pairing of their matrix representations

$$\langle\!\langle \tau | \sigma \rangle\!\rangle = \langle\!\langle \tau_{ij} dx^i dx^j | \sigma^{k\ell} \mathbf{e}_k \mathbf{e}_\ell dA \rangle\!\rangle = \tfrac{1}{2} \int_{\mathbb{R}^2} \sum_{ij} \tau_{ij} \sigma^{ij} dA, \tag{2.12}$$

and the dual pairing between $\mathbf{f} \in \Gamma(T\mathbb{R}^2 \otimes \wedge^2 T^*\mathbb{R}^2)$ and $\alpha \in \Gamma(T^*\mathbb{R}^2)$ is given by

$$\langle\!\langle \alpha | \mathbf{f} \rangle\!\rangle = \langle\!\langle \alpha_i dx^i | f^j \mathbf{e}_j dA \rangle\!\rangle = \int_{\mathbb{R}^2} \sum_i \alpha_i f^i dA. \tag{2.13}$$

Using this establishment of the duality relation, we can describe the solvability of the

linear constraint in (2.9)

$$\text{div}\,\sigma = \mathbf{f}. \qquad (2.14)$$

The linear constraint (2.14) admits a solution σ if and only if $\mathbf{f} \in \text{im}(\text{div}) = \ker(\mathscr{K})^{\perp}$ where $(\cdot)^{\perp}$ denotes the annihilator space. Note that the kernel of the operator $\mathscr{K}$ is the collection of the $\flat_{\mathbb{R}^2}$ of Killing vector fields, which generate isometric flows on the domain. On $\mathbb{R}^2$, these Killing vector fields are the generators for rigid body transformations. In particular, $\ker(\mathscr{K}) = \text{span}\{dx, dy, xdy - ydx\}$, where $(x, y) = (x^1, x^2)$. Therefore, we have the following characterization for the valid $\mathbf{f}$ for (2.14).

Theorem 1 *Eq.* (2.14) *admits a solution* σ *if and only if the prescribed force distribution* $\mathbf{f} = f_i \mathbf{e}^i dA$ *satisfies the conditions of vanishing net force and vanishing total torque*

$$\begin{cases} \int_{\mathbb{R}^2} f_1\, dA = 0 \\[2mm] \int_{\mathbb{R}^2} f_2\, dA = 0 \\[2mm] \int_{\mathbb{R}^2} (xf_2 - yf_1)dA = 0. \end{cases} \qquad (2.15)$$

In our problem, we assume that the prescribed force distribution $\mathbf{f}$ satisfies the physically intuitive necessary and sufficient conditions (2.15). Even if we are handed in with a force distribution $\mathbf{f}$ that violates (2.15), it is straightforward to project it to fulfill the conditions by adding a suitable rigid motion vector field.

2.3.2 Representing Tensors and Differential Operators

We can represent symmetric tensors as arrays of their matrix elements. For instance, in the 2×2 case, a tensor with elements σ_{ij} can be represented as a vector $(\sigma_{11}, \sigma_{22}, \sigma_{12})^{\mathsf{T}} \in \mathbb{R}^3$. In Figure 2.5, we use this $\mathbb{R}^3$ representation to depict the unit ball under our spectral p-norm as well as the image of $\mathbf{G}(1, \mathbb{R}^2)$ under the Veronese map $\mathscr{V}$. By representing a symmetric matrix

using these coordinates, the dual pairing (2.12) becomes

$$\langle\!\langle \tau | \sigma \rangle\!\rangle = \int_{\mathbb{R}^2} \begin{bmatrix} \tau_{11} & \tau_{22} & \tau_{12} \end{bmatrix} \begin{bmatrix} 1/2 & & \\ & 1/2 & \\ & & 1 \end{bmatrix} \begin{bmatrix} \sigma_{11} \\ \sigma_{22} \\ \sigma_{12} \end{bmatrix} dA, \qquad (2.16)$$

and the differential operators div and $\mathcal{K}$ can be written as matrices of differential operators:

$$\mathrm{div} = \begin{bmatrix} \partial_x & & \partial_y \\ & \partial_y & \partial_x \end{bmatrix}, \quad \mathcal{K} = \begin{bmatrix} 2\partial_x & \\ & 2\partial_y \\ \partial_y & \partial_x \end{bmatrix}. \qquad (2.17)$$
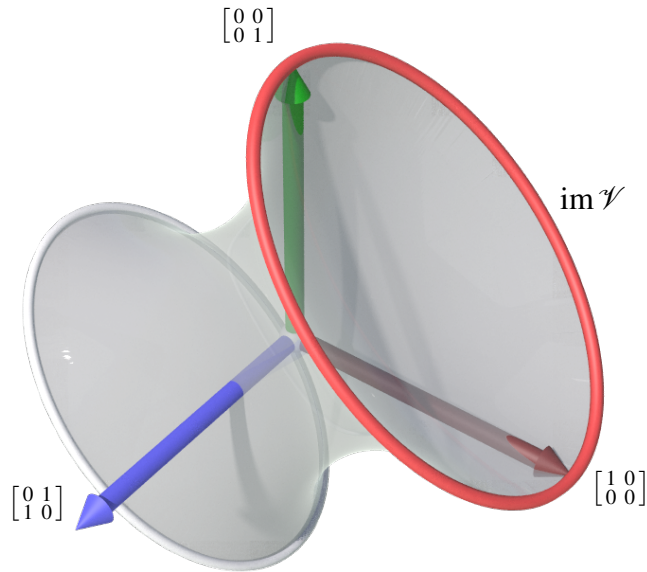

Figure 2.5. The $|\cdot|_p$ unit ball (grey), and the image of the Veronese map (red) in the 3-dimensional space of symmetric 2×2 matrices. Solutions tend towards the sharp rims of this unit ball.

2.3.3 Obstacles

An extension to our optimization problem (2.9) allows us to construct varifolds which avoid "obstacles" placed in the domain. Let $w : \mathbb{R}^2 \to \mathbb{R}_{>0}$ be a function over the base space $\mathbb{R}^2$

which takes the value 1 on obstacle-free areas of the domain, and takes the value $B \gg 1$ on areas filled with obstacle. Then the objective

$$\underset{\sigma}{\text{minimize}} \int_{\mathbb{R}^2} w|\sigma|_p^q dA \quad \text{subject to div}\,\sigma = \mathbf{f} \tag{2.18}$$

encourages solutions to avoid obstacles. Given large enough B, solutions tend to pass around the obstacle-filled regions.

2.4   Algorithm

In this section, we describe an optimization algorithm equivalent to applying the Linearized Augmented Lagrangian Method [30] to our problem. This algorithm is best described as a Backward Euler discretization of a continuous gradient flow that optimizes the objective. The backward Euler steps are further translated into a sequence of variational problems using the method of incremental potential [15, 3, 13].

The aforementioned constrained optimization problem (2.18) takes the minimax form

$$\min_{\sigma} \max_{\lambda} \int_{\mathbb{R}^2} w|\sigma|_p^q dA + \int_{\mathbb{R}^2} \langle \lambda \,|\, \text{div}\,\sigma - \mathbf{f} \rangle \tag{2.19}$$

where the type of the Lagrange multiplier λ is $\Gamma(T^*\mathbb{R}^2)$. The optimal solution can be found by following the coupled gradient descent and ascent flows with respect to σ and λ. These continuous gradient flows are

$$\begin{cases} G_1 \frac{\partial \sigma}{\partial t} = -w \frac{\partial |\sigma|_p^q}{\partial \sigma} + \mathcal{K}\lambda \\ G_2 \frac{\partial \lambda}{\partial t} = \text{div}\,\sigma - \mathbf{f} \end{cases} \tag{2.20}$$

where G_1, G_2 are linear operators describing metrics for the space $\Gamma(T\mathbb{R}^2 \otimes_{\text{sym}} T\mathbb{R}^2 \otimes \wedge^2 T^*\mathbb{R}^2)$ of primal variables σ and the space $\Gamma(T^*\mathbb{R}^2)$ of Lagrange multipliers λ, respectively. These

metrics will be chosen suitably later during our derivation.

We discretize the flow (2.20) temporally using the backward Euler method. Replace the time derivatives $\frac{\partial(\cdot)}{\partial t}$ by $\frac{(\cdot)^{(n+1)} - (\cdot)^{(n)}}{\Delta t}$ with a step size Δt, evaluate the right-hand sides of (2.20) at time step $(\cdot)^{(n+1)}$, and approximate $\lambda^{(n+1)}$ on the right-hand side by $\lambda^{(n+1)} \approx \lambda^{(n)} + \Delta\lambda^{(n)}$ using $\Delta\lambda^{(n)} = \lambda^{(n)} - \lambda^{(n-1)}$ from the previous step to avoid a joint root finding system. The equations become:

$$G_1 \frac{\sigma^{(n+1)} - \sigma^{(n)}}{\Delta t} = -w\left(\frac{\partial|\sigma|_p^q}{\partial\sigma}\right)^{(n+1)} + \mathscr{K}\left(\lambda^{(n)} + \Delta\lambda^{(n)}\right), \qquad (2.21a)$$

$$G_2 \Delta\lambda^{(n+1)} = \Delta t\left(\operatorname{div}\sigma^{(n+1)} - \mathbf{f}\right), \qquad (2.21b)$$

$$\lambda^{(n+1)} = \lambda^{(n)} + \Delta\lambda^{(n+1)}. \qquad (2.21c)$$

Let

$$z^{(n+1)} := \sigma^{(n)} + \Delta t\, G_1^{-1} \mathscr{K}\left(\lambda^{(n)} + \Delta\lambda^{(n)}\right), \qquad (2.22)$$

which simplifies (2.21a) into

$$\frac{1}{\Delta t} G_1\left(\sigma^{(n+1)} - z^{(n+1)}\right) + w\left(\frac{\partial|\sigma|_p^q}{\partial\sigma}\right)^{(n+1)} = 0. \qquad (2.23)$$

Solving (2.23) is equivalent to solving the optimization problem

$$\sigma^{(n+1)} = \operatorname*{argmin}_{\sigma} \frac{1}{2\Delta t}\|\sigma - z^{(n+1)}\|_{G_1}^2 + \int_{\mathbb{R}^2} w|\sigma|_p^q dA. \qquad (2.24)$$

We choose G_1 as the L^2 Frobenius metric $\|\sigma\|_{G_1}^2 := \int_{\mathbb{R}^2} \sum_{ij} \sigma_{ij}^2 dA$. Effectively, G_1 is the identity map on the tensor coefficients; in particular, we can omit G_1 in (2.21a) and (2.22). With this choice of L^2 Frobenius metric, the sub-optimization problem (2.24) has an explicit solution given as a local *shrinkage step* on singular values [30]: Let $U\Sigma V^\mathsf{T}$ be the singular value decomposition

for $z^{(n+1)}$; then the solution to (2.24) is

$$\sigma^{(n+1)} = U \max\left(\Sigma - w\Delta t \, pq\Sigma^{\frac{(p-1)(q-1)}{p}}, 0\right) V^\mathsf{T}. \tag{2.25}$$

Finally, to complete (2.21) we choose the metric G_2. Observe that combining (2.22) and (2.21b) yields an expression that involves adding to $\sigma^{(n)}$ by a term $\Delta t^2 \mathcal{K} G_2^{-1} \operatorname{div}\sigma^{(n)}$. To better precondition this update, we note that G_2 should be chosen to "cancel out" the derivatives $\mathcal{K}$ and div. Thus a good choice is $G_2 = -\mu \operatorname{div}\circ\mathcal{K} = \mu \operatorname{div}\operatorname{div}^*$ for any scale factor $\mu > 0$.

We obtain our final algorithm:

Algorithm 1. Minimax flow with backward Euler method

1: $z^{(n+1)} \leftarrow \sigma^{(n)} + \Delta t \mathcal{K}(\lambda^{(n)} + \Delta\lambda^{(n)})$

2: $\sigma^{(n+1)} \leftarrow$ Eq. (2.25)

3: $\Delta\lambda^{(n+1)} \leftarrow \frac{\Delta t}{\mu}(-\operatorname{div}\mathcal{K})^{-1}(\operatorname{div}\sigma^{(n+1)} - \mathbf{f})$

4: $\lambda^{(n+1)} \leftarrow \lambda^{(n)} + \Delta\lambda^{(n+1)}$

Our algorithm matches the Linearized Augmented Lagrangian Method for our optimization problem [30].

Spectral method for $\mathcal{K}$ and div

To invert and apply differential operators like div and $\mathcal{K}$ to tensors, we can take the Fast Fourier Transform (FFT) to these tensors defined on a rectangular domain of size $L_1 \times L_2$ with periodic boundary condition. FFT converts each partial derivative ∂_i to $\hat{\imath}\frac{2\pi k_i}{L_i}$, where k_i is the integer index in the Fourier domain in the i-th direction. All div and $\mathcal{K}$ operations (2.17) as well as $(-\operatorname{div}\mathcal{K})^{-1}$ can thus be performed in the Fourier domain as frequency-wise small complex matrices. An artifact of this procedure is the introduction of periodic boundary conditions on our domain; however, these can be nullified by placing boundary obstacles using our method.

2.5 Results

We implement[3] our algorithm in VEX in Houdini FX 18.5. All results were computed using a grid with resolution 256×256, a constant large time step $\Delta t = \mu = 30$, a fixed exponent $p = q = {}^1\!/_2$ (except for an ablation study), and 500 iterations. The computation were performed on a 2019 MacBook Air using a 1.6 GHz Dual-Core Intel Core i5. Each iteration takes about $40\,\mathrm{ms}$ with the FFT being the main bottleneck.[4] That is, each example is obtained within 20 seconds.

tension   compression

0.0
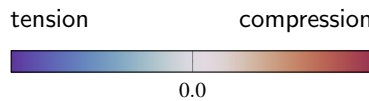
Figure 2.6. The sign of the only nonzero eigenvalue of the stress tensor represents tension or compression.

The visualization of the results shows the trace of the stress tensor σ at each grid cell. When σ at a cell is rank 1 (*i.e.* it is in the image of the Veronese map), this trace shows the value of the only nonzero eigenvalue of σ. Blue strands represent tension, and can be interpreted as cables; red strands represent compression, interpreted as struts.

2.5.1 Numerical Tests, Validation, and Ablation

Single cable

Consider a simple setup where the force distribution is given by two impulses on two points, and the force vector points radially away from each other (Fig. 2.7). The optimal support structure mediating this force distribution is the line segment joining the two points, representing a cable pulled by the forces. Fig. 2.7 shows the result of our algorithm over a few iterations, demonstrating that our method successfully reproduces a sharp line segment connecting the given points.

---

[3]The implementation is included in the supplementary material.
[4]This performance is without any GPU acceleration.

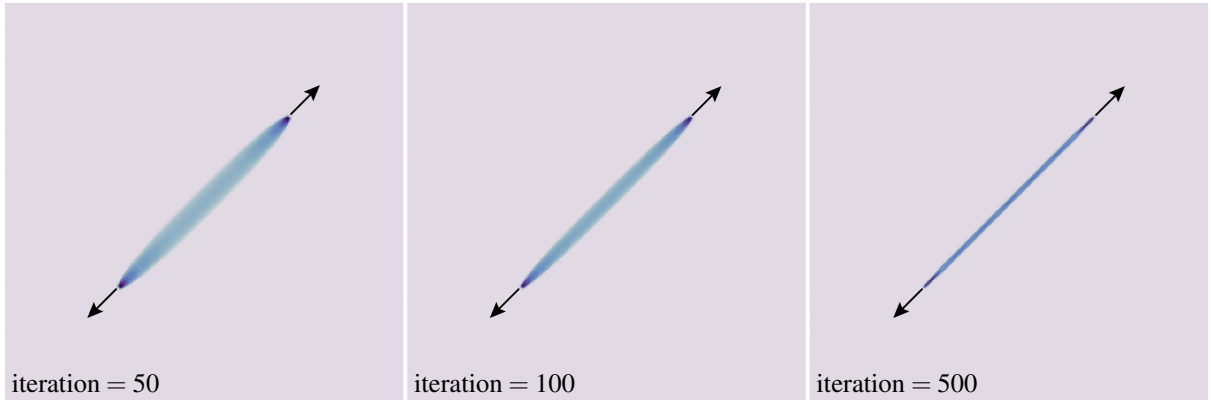**Figure 2.7.** A cable emerges as the result of running our algorithm for 500 iterations on **f** defined on two points, pointing radially outward.

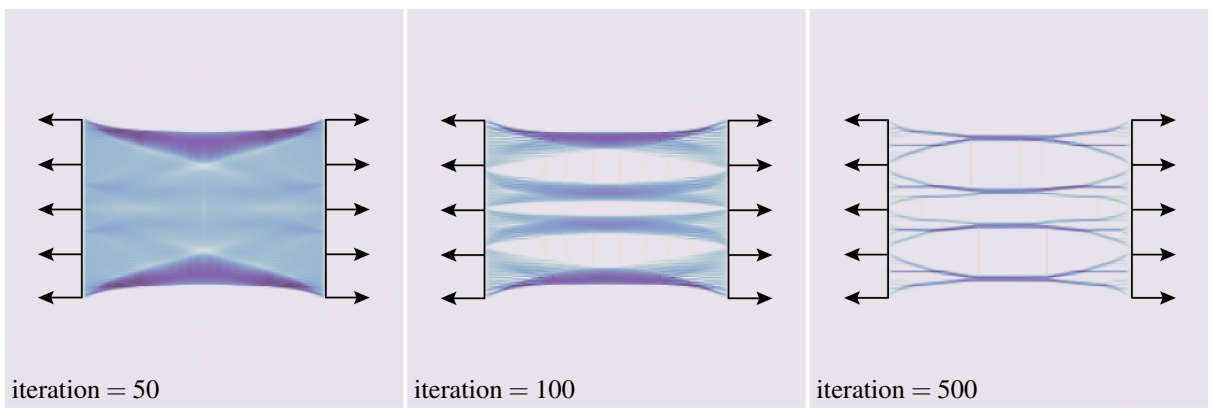**Figure 2.8.** The result of running our algorithm for 500 iterations on **f** evenly distributed on two sheets, pointing horizontally away from the center line. See also Fig. 2.9.
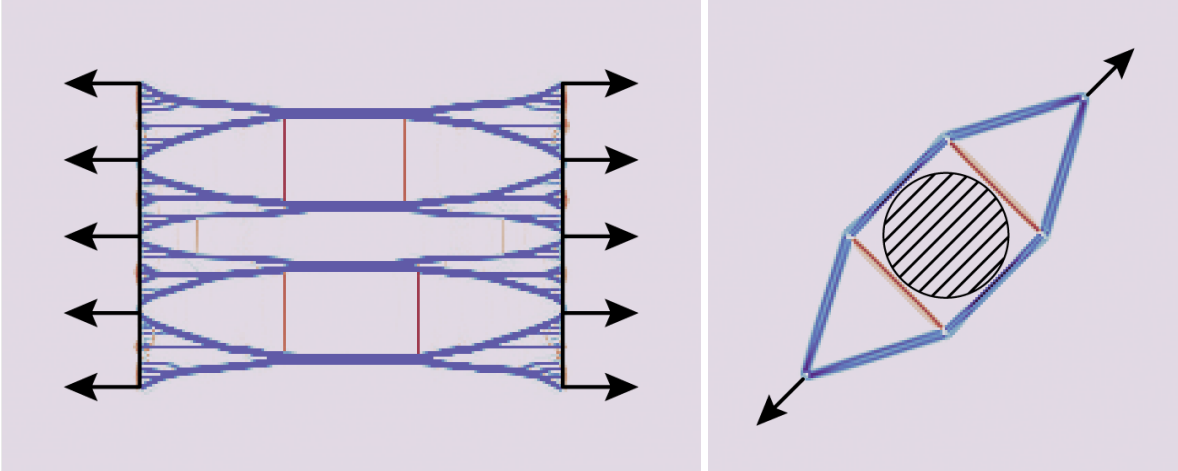
Figure 2.9. Sparse support structures found by our algorithm. Left: The force is set to evenly distribute over two sheets; this is the same result shown in Fig. 2.8 but the color axis is rescaled to display detailed support structures. Right: Pair of point forces with an obstacle (shaded region) blocking in between the points (*cf.* Fig. 2.2).

Force sheets

Instead of prescribing forces concentrated on point sets, we test our algorithm for force distributed over one-dimensional sets. Fig. 2.8 shows the result of our algorithm when the force is evenly distributed over two sheets facing each other. Despite the denseness of the force distribution, our method is able to find a sparse network of cables and struts supporting the given load. After a tone mapping, Fig. 2.9 (left) reveals the emergent detailed branches and reinforcement structure.

Obstacle

Fig. 2.9 (right) shows the setup of Section 2.5.1 with an additional circular obstacle placed in between the points, similar to the illustration Fig. 2.2. The obstacle is prescribed through a large weight $w = 1000$ in the obstacle and $w = 1$ elsewhere. The algorithm finds a realistic structure which avoids the obstacle.

We also test the algorithm for a more challenging obstacle configuration. In Fig. 2.12, we place a large obstacle in between the force sheets of Fig. 2.8. The algorithm automatically finds a shockingly sophisticated system of cables and struts to wrap around the obstacle, held together
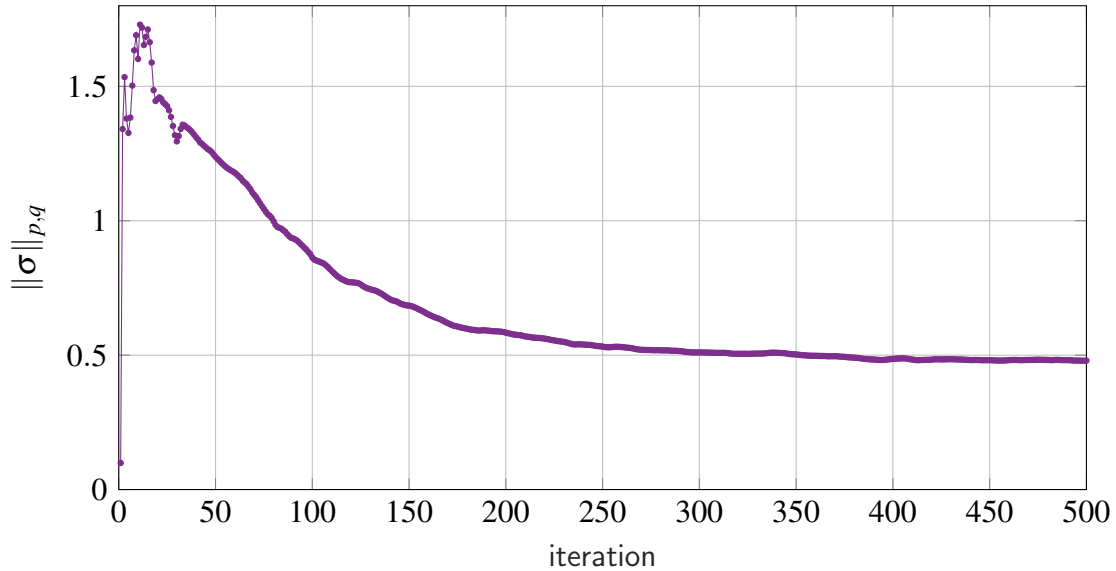
Figure 2.10. The convergence of the loss function in the example of Fig. 2.8.

by emergent "tied arch bridges" reaching beyond the convex hull of the support of the force.

Convergence

Fig. 2.10 shows a typical convergence plot of the loss function for our algorithm. Note that there is no procedure in the optimization such as line-search that would shrink the optimization step size Δt. With a fixed step size, the plot reflects an asymptotic stability of the flow (2.20).

(p,q) **dependency**

Fig. 2.11 shows the force sheet setup for several combinations of parameters p and q in our (p,q)-spectral norm. In general, small q enforces global sparsity, while small p enforces local low-rank quality. In the case when $p = q = 1$, our objective reduces to L^1–nuclear norm minimization, and our solutions do not achieve the same sparsity. For all other experiments, we choose $p = q = {}^1\!/_2$.

2.5.2 Miscellaneous Examples

Bridge Designs

We test that our algorithm is able to generate reasonable results for common engineering problems. Fig. 2.13 shows our algorithm's output for a force distribution on a horizontal "road" applying uniform downward force, with two point support forces a distance below the road. A rectangular obstacle is placed a small distance below the road, to allow for vehicles or pedestrians to pass under the resulting structure. Our algorithm identifies an arch of struts with attached cables, similar to a real-world bridge design.

A similar setup is tested in Fig. 2.14, with a longer road, a thinner obstacle, and upward point forces a further distance below the road. Under these conditions, our algorithm generates a more organic bridge structure. This result is also presented in Fig. 2.1.

Fig. 2.15 demonstrates another setup with two roads stacked vertically. Our algorithm generates a hybrid arch-suspension bridge with one tall arch.

Cantilever Beam

The *cantilever beam* is a common test case in topology optimization research. In Fig. 2.16, we design a similar setup by placing a weight force at the end of a beam, and balancing forces on the other end representing points where the beam attaches to a wall. Our algorithm develops a series of curved cables and struts which support the weight at the end of the beam. These results appear similar to outputs from standard topology optimization routines.

2.6   Conclusion and Discussion

We develop an optimization algorithm which employs geometric measure theoretic techniques to find a sparse network of (potentially non-manifold) curves connecting a prescribed force distribution over a given domain. We have shown that our algorithm handles complex force distributions with obstacles in the domain using a series of Fast Fourier Transform and shrinkage
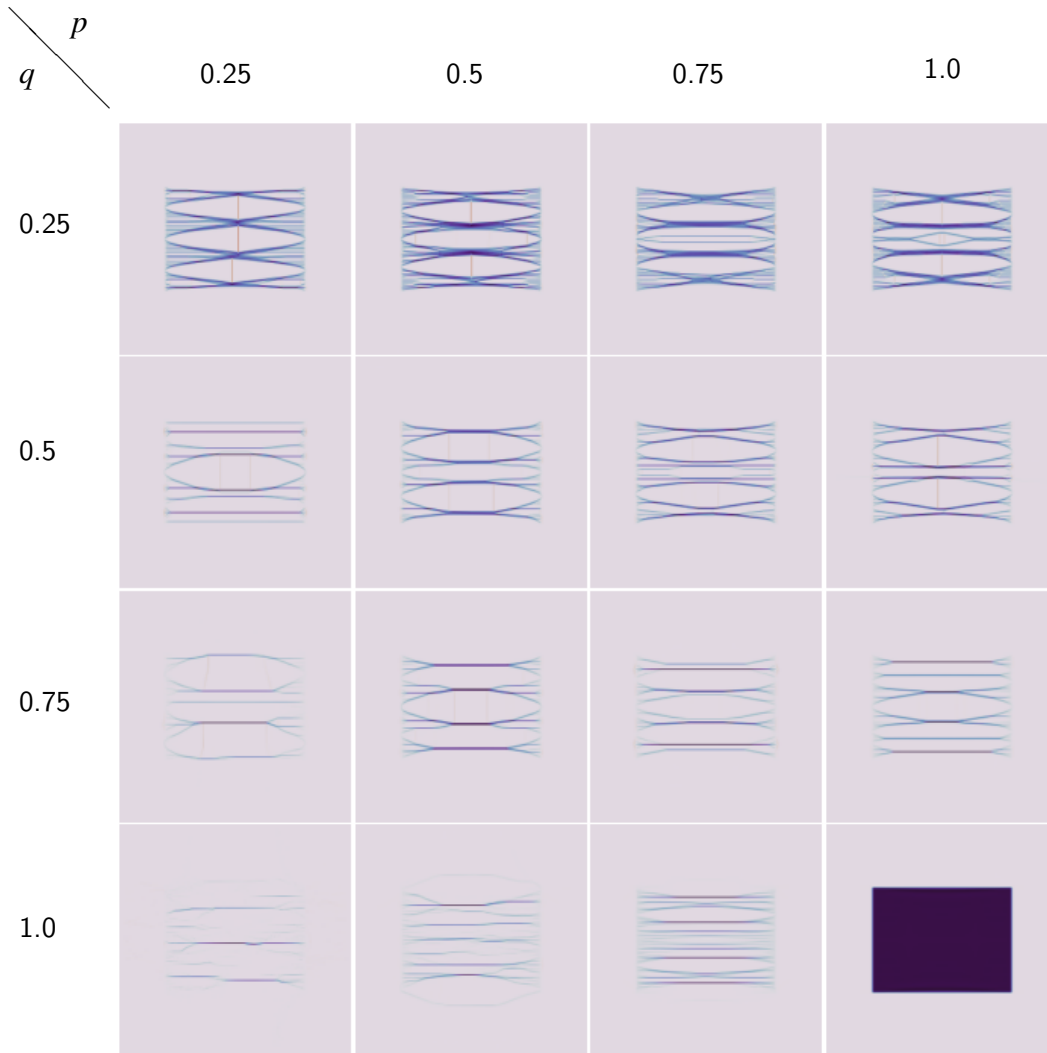
22

Figure 2.11. The result of our algorithm for the "bars" $\mathbf{f}$ for varying p, q in the objective.

steps. With the Fast Fourier Transform in our algorithm being the most costly step, we obtain each result less than half a minute.

Though each solution obtained from our algorithm provides a physically plausible design, the method still demands rigorous theoretical guarantees. We have not proven convergence properties for our non-convex optimization problem. It is likely that concrete statements about convergence can be made by analyzing our Sobolev gradient flow. Moreover, we have not shown the mechanical stability of our results in addition to the equilibrium condition, though we speculate that our variational approach to the problem may imply stability.
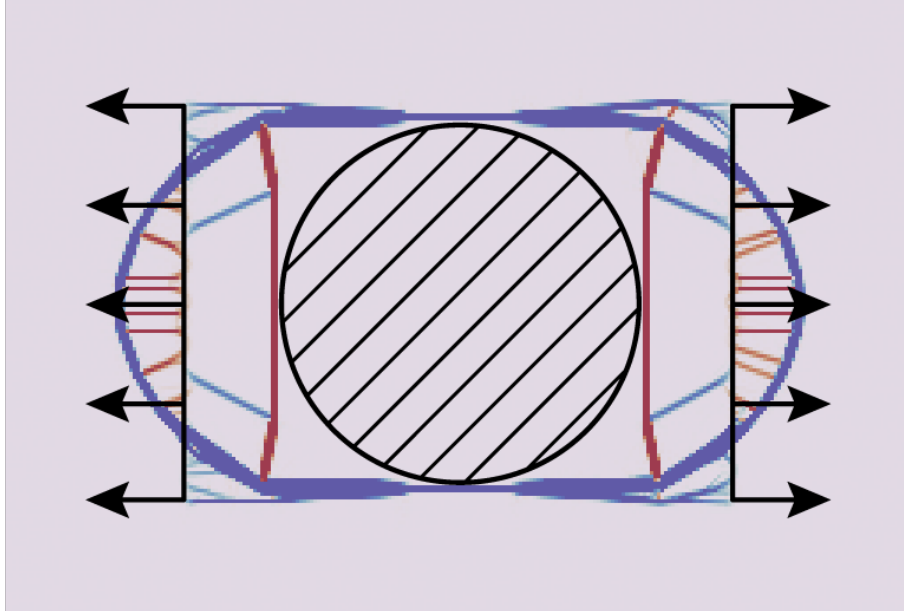
Figure 2.12. A stress-minimizing structure for the same **f** distribution as in Fig. 2.8, but now with an additional disk obstacle between the force sheets. The algorithm avoids the obstacle and constructs "tied arch bridges" to maintain the stress-free condition.

We also note that our (p, q)-spectral norm minimization formulation is only a non-convex continuous relaxation of the original combinatorial graph minimization problem. This can lead to suboptimal solutions in comparison to known minimal graphs (Fig. 2.17). It would be interesting to draw relation between our minimal stress reconstruction problem to the Steiner tree problem and the branched optimal transport problem [29, 2, 19].

The scope of this paper is limited to 2 dimensions with a Euclidean metric. Extending the theory to respect arbitrary Riemannian metrics requires replacing the derivatives in (2.5b) and (2.10b) by covariant derivatives, compromising the diagonalizability by Fourier Transform. Additionally, a 3-dimensional version of our algorithm has yet to be experimented thoroughly. Higher dimensions introduce visualization and storage challenges. These challenges can likely be resolved using techniques of [14] or [17].

Finally, our treatment's use of low-rank stress tensors as varifolds opens new avenues in geometric measure theory. We hope that this physical representation and interpretation leads to further developments in computational applications of geometric measure theory.
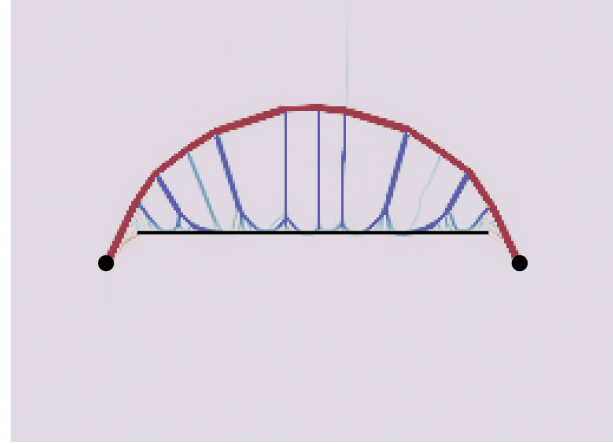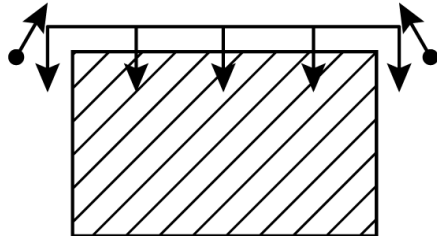
Figure 2.13. A tied arch bridge discovered by our algorithm. **f** points downward on a horizontal "road", and points northeast and northwest at the lower left and lower right points respectively. An obstacle is placed in the bottom center, to allow boats or highways to pass under the bridge.

Chapter 2, in full, has been submitted for publication of the material as it may appear in ACM Transactions on Graphics (TOG)—Proceedings of ACM SIGGRAPH Asia, 2023, Rowe, Dylan; Chern, Albert. The thesis author was the primary investigator and author of this paper.
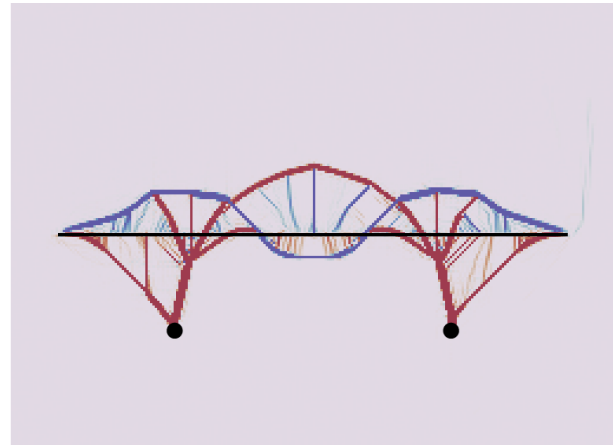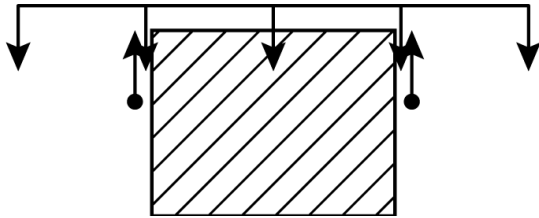
Figure 2.14. A hybrid suspension-tied arch bridge discovered by our algorithm. The horizontally distributed downward force represents a road, and two upward forces at the two lower points represent supports. An obstacle is placed in the bottom center to allow boats or highways to pass under the bridge.
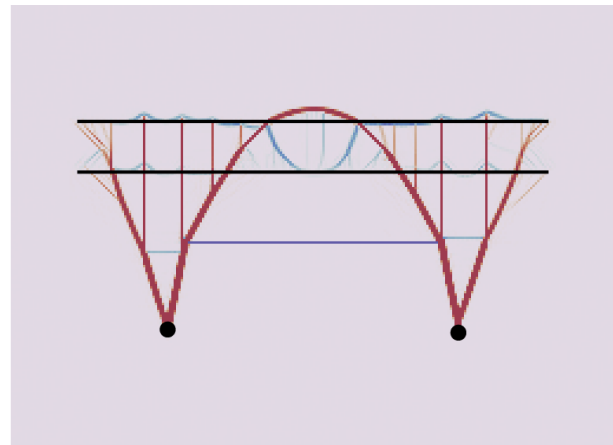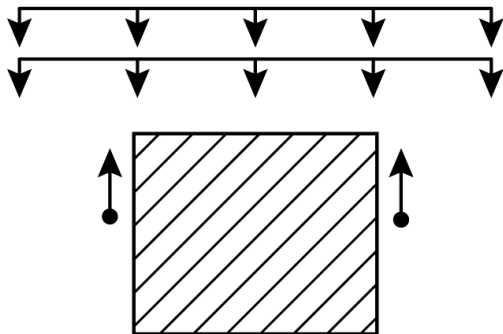

Figure 2.15. A hybrid arch-suspension bridge discovered by our algorithm. **f** represents the weight from two decks of roads, and normal force from two supports. There is a rectangular obstacle in the bottom center.
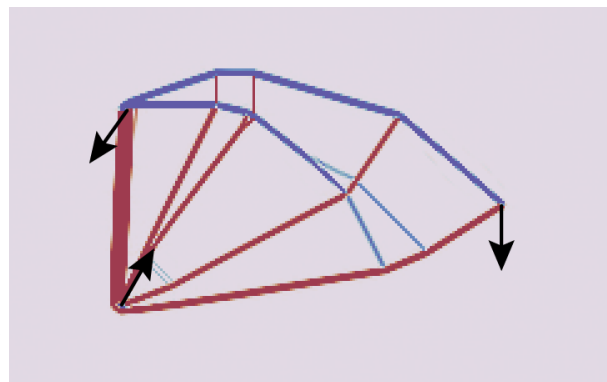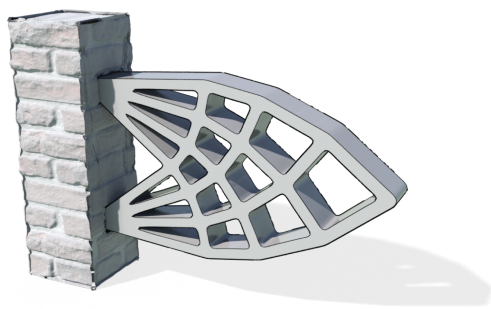
Figure 2.16. The cantilever beam problem (left) is a common topology optimization test case. Our result (right) reproduces a pattern similar to the iconic Michell structure (left). We believe our algorithm can be used as a lightweight preprocessing step for more costly topology optimization methods.
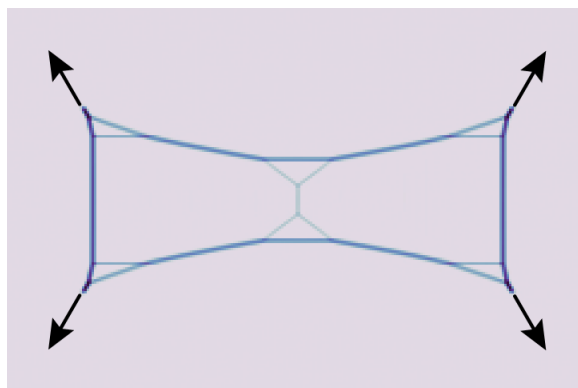

Figure 2.17. Effect of our continuous relaxation to the original graph minimization problem. The result of our algorithm (right) for 4 point forces, pointing at $60°$ from the horizontal at each point, is a sparse graph that deviates from the classical minimal Steiner tree (left).

Chapter 3

Additional Results

3.1 Introduction

This section contains additional results not part of the original paper.

3.2 Circle

Our algorithm gives interesting and nontrivial results on a circular force distribution, with forces pointing outwards radially. The most interesting results arise in the low-q regime (*i.e.* in Fig. 3.1), where rich structures form in the interior of the circular distribution, reminiscent of axis-aligned snowflakes. Fig. 3.2 studies outputs for varying p and q.
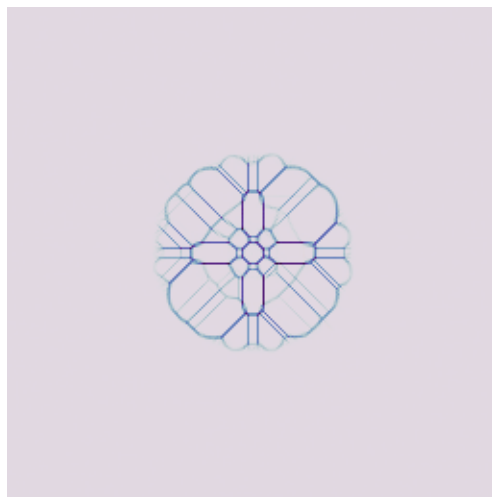

Figure 3.1. The result of our algorithm on a circular force distribution for $p = 1, q = 0.25$.
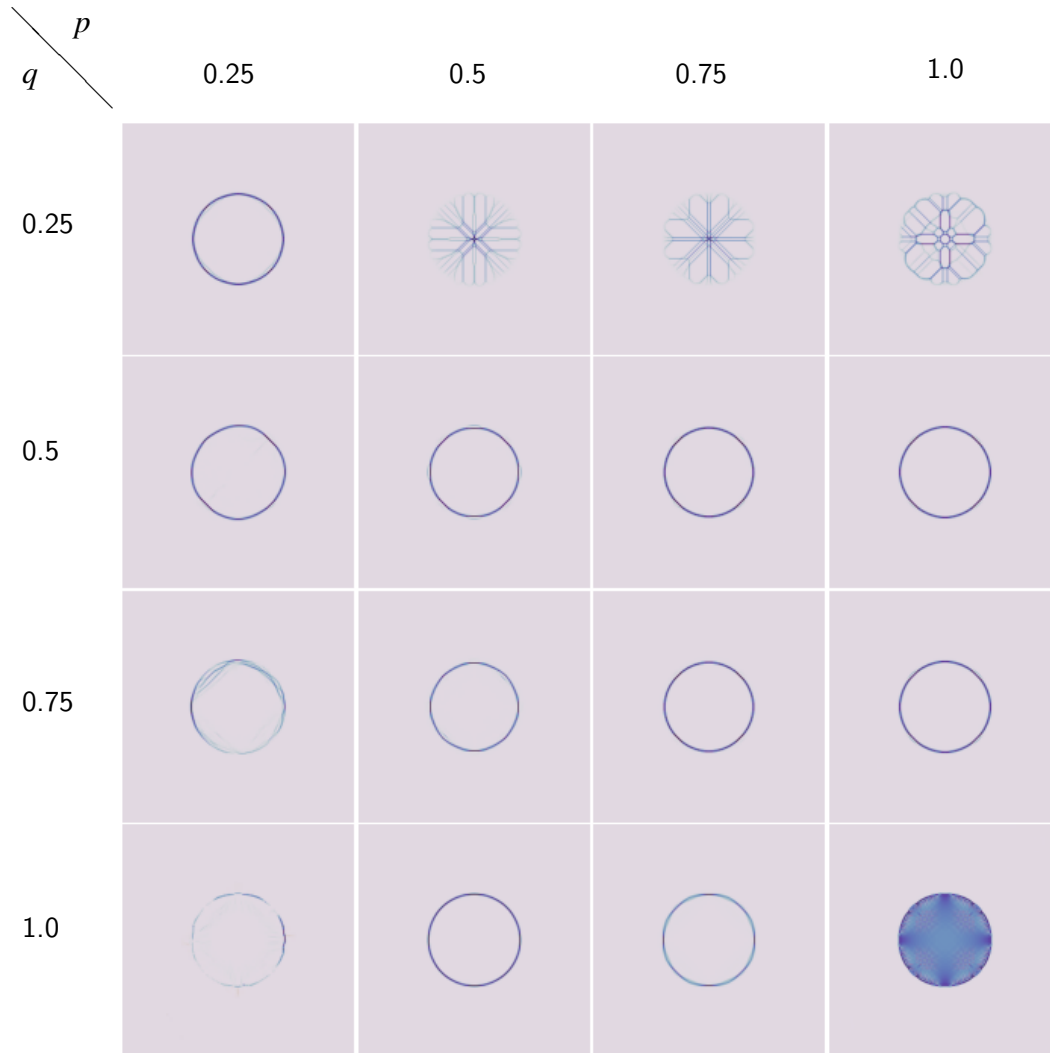
Figure 3.2. The result of our algorithm for a circular force distribution **f** for varying p, q in the objective.

3.3 Further Evidence of Sparsity

The trace is useful as an indicator of the first eigenvalue of the stress tensor only when the stress tensor is known to be rank 1. Here, we visualize the results of the same optimization process shown in Fig. 2.8, but using the determinant of the stress tensor, which is the product of the eigenvalues, rather than the sum. When the determinant is 0, the stress tensor at that point is low rank. Otherwise, the stress tensor will be full rank. In Fig. 3.3, it is evident that our optimization process encourages low rank stress tensors – at iteration 50, the rank is full in many
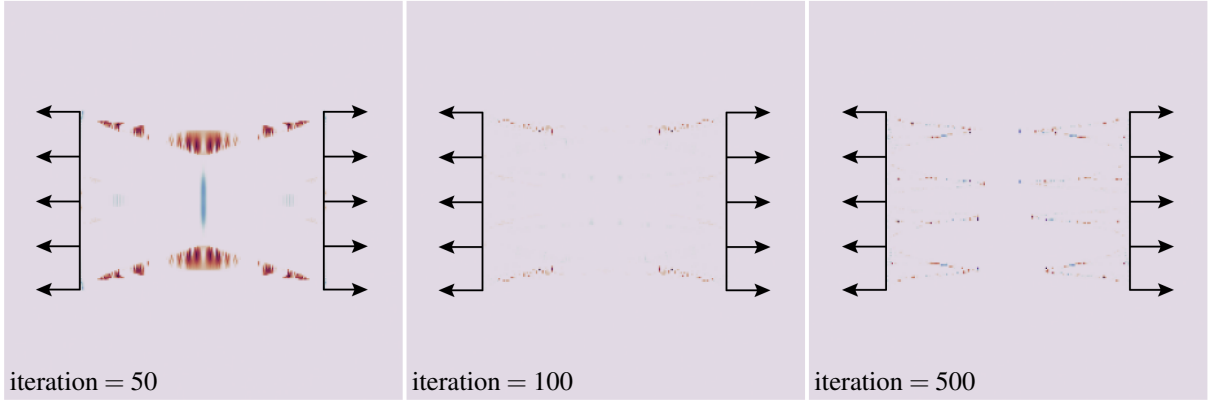
| iteration = 50 | iteration = 100 | iteration = 500 |

Figure 3.3. The same setup as Fig. 2.8, but visualizing the determinant rather than the trace of the stress tensor.

parts of the structure; at iteration 500, the rank is full only at a few points.

3.4   Solutions on the p, q-spectral Unit Ball

By mapping individual symmetric tensors in the algorithm's output to 3 dimensions using the coordinates described in Chapter 2, we can visualize the solutions' coalescence at the rims of the unit ball. Here, solutions from the force sheets (depicted in the final frame of Fig. 2.8) and diagonal points (shown in the final frame of Fig. 2.7) are converted to point sets which are then projected onto the unit ball to normalize the scales of each tensor. Then, the alpha value of each point is normalized by the maximum p, q-norm in the dataset. It is clear that solutions tend towards the rims of the unit ball, as predicted. Fig. 3.4 shows the output of this process for the force sheet distribution, whereas Fig. 3.5 shows the output for the diagonal points.

3.5   Three Dimensional Results

It is natural to ask what happens to our algorithm when moving to the third dimension. Below, the results of running our algorithm with analogous parameters are shown. Fig. 3.6 shows an isosurface of the Frobenius norm of the stress tensor at 50, 100, and 500 iterations for a distribution at two points with force pointing radially outward. Fig. 3.7 and Fig. 3.8 show the same visualization for a distribution of 8 points on the corners of a cube. Rich and sparse
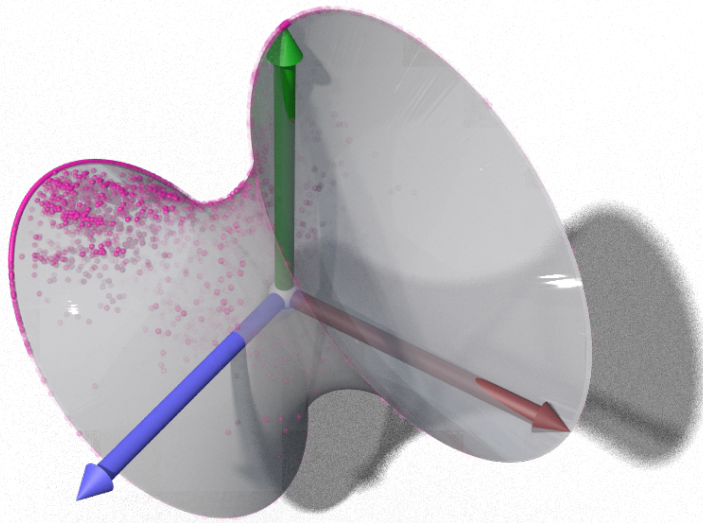
Figure 3.4. Tensors in the "force sheets" distribution tend towards the rims of the unit ball.
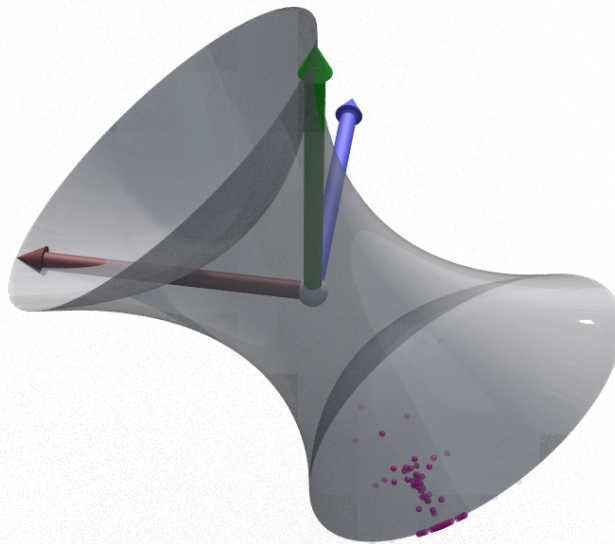

Figure 3.5. Tensors in the "diagonal points" distribution prefer a specific spot on the backside of the unit ball; note the camera rotation.

Figure 3.6. Optimization of a distribution analogous to the diagonal points force distribution in 2 dimensions. An isosurface is shown at 50, 100, and 500 iterations (from left to right).
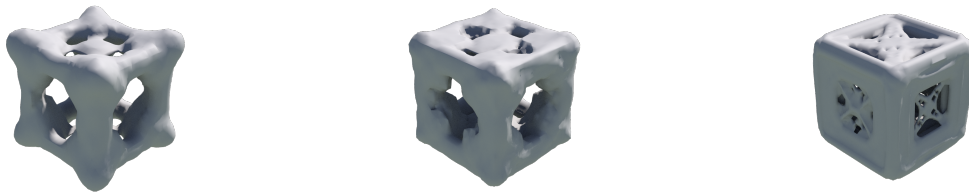
Figure 3.7. Optimization of a force distribution situated at the corners of a cube, pointing radially outward. An isosurface of the Frobenius norm of the stress tensor is shown at 50, 100, and 500 iterations (from left to right).

structures form at the faces of the cube, but the structures change as the isosurface threshold changes, and smoke/cloud visualizations do not show such structures at the same strength. Visualization and experimentation with this extension is thus left to future work.

Figure 3.8. The final image (iteration 500) from Fig. 3.7, expanded to highlight the internal detail.

Bibliography

[1] Marcel Berger and D Ebin. Some decompositions of the space of symmetric tensors on a riemannian manifold. *Journal of Differential Geometry*, 3(3-4):379–392, 1969.

[2] Mauro Bonafini, Giandomenico Orlandi, and Édouard Oudet. Variational approximation of functionals defined on 1-dimensional connected sets: the planar case. *SIAM Journal on Mathematical Analysis*, 50(6):6307–6332, 2018.

[3] Sofien Bouaziz, Sebastian Martin, Tiantian Liu, Ladislav Kavan, and Mark Pauly. Projective dynamics: Fusing constraint projections for fast simulation. *ACM transactions on graphics (TOG)*, 33(4):1–11, 2014.

[4] Blanche Buet, Gian Paolo Leonardi, and Simon Masnou. A varifold approach to surface approximation. *Archive for Rational Mechanics and Analysis*, 226(2):639–694, jun 2017.

[5] Nicolas Charon and Alain Trouvé. The varifold representation of non-oriented shapes for diffeomorphic registration. *CoRR*, abs/1304.6108, 2013.

[6] Fernando de Goes, Beibei Liu, Max Budninskiy, Yiying Tong, and Mathieu Desbrun. Discrete 2-tensor fields on triangulations. In *Computer Graphics Forum*, volume 33, pages 13–24. Wiley Online Library, 2014.

[7] Joshua D. Deaton and Ramana V. Grandhi. A survey of structural and multidisciplinary continuum topology optimization: Post 2000. *Struct. Multidiscip. Optim.*, 49(1):1–38, jan 2014.

[8] Shintaro Ehara and Yoshihiro Kanno. Topology design of tensegrity structures via mixed integer programming. *International Journal of Solids and Structures*, 47(5):571–579, 2010.

[9] Richard Buckminster Fuller. Tensile-integrity structures, US3063521A, Nov. 1962.

[10] Valentin Gomez-Jauregui. *Tensegrity structures and their application to architecture*. PhD thesis, 09 2004.

[11] Albert Graells Rovira and Josep M. Mirats Tur. Control and simulation of a tensegrity-based mobile robot. *Robotics and Autonomous Systems*, 57(5):526–535, 2009.

[12] Donald E Ingber. Tensegrity i. cell structure and hierarchical systems biology. *J. Cell Sci.*, 116(Pt 7):1157–1173, April 2003.

[13] Minchen Li, Zachary Ferguson, Teseo Schneider, Timothy R Langlois, Denis Zorin, Daniele Panozzo, Chenfanfu Jiang, and Danny M Kaufman. Incremental potential contact: intersection-and inversion-free, large-deformation dynamics. *ACM Trans. Graph.*, 39(4):49, 2020.

[14] Haixiang Liu, Yuanming Hu, Bo Zhu, Wojciech Matusik, and Eftychios Sifakis. Narrow-band topology optimization on a sparsely populated grid. *ACM Transactions on Graphics (TOG)*, 37(6), 2018.

[15] Sebastian Martin, Bernhard Thomaszewski, Eitan Grinspun, and Markus Gross. Example-based elastic materials. In *ACM SIGGRAPH 2011 papers*, pages 1–8. 2011.

[16] J.W. Milnor and J.D. Stasheff. *Characteristic Classes*. Annals of mathematics studies. Princeton University Press, 1974.

[17] David Palmer, Dmitriy Smirnov, Stephanie Wang, Albert Chern, and Justin Solomon. DeepCurrents: Learning implicit representations of shapes with boundaries. In *Proceedings of the IEEE/CVF Conference on Computer Vision and Pattern Recognition (CVPR)*, 2022.

[18] C. Paul, F.J. Valero-Cuevas, and H. Lipson. Design and control of tensegrity robots for locomotion. *IEEE Transactions on Robotics*, 22(5):944–957, 2006.

[19] Paul Pegon, Filippo Santambrogio, and Qinglan Xia. A fractal shape optimization problem in branched transport. *Journal de Mathématiques Pures et Appliquées*, 123:244–269, 2019.

[20] S. Rajeev and C. S. Krishnamoorthy. Genetic algorithms-based methodology for design optimization of trusses. 1997.

[21] G. I. N. Rozvany. A critical review of established methods of structural topology optimization. *Structural and Multidisciplinary Optimization*, 37(3):217–237, 2009.

[22] Ole Sigmund and Kurt Maute. Topology optimization approaches. *Structural and Multidisciplinary Optimization*, 48(6):1031–1055, 2013.

[23] Anthony So and Yinyu Ye. A semidefinite programming approach to tensegrity theory and realizability of graphs. pages 766–775, 01 2006.

[24] Anthony Man-Cho So and Yinyu Ye. Theory of semidefinite programming for sensor network localization. *Mathematical Programming*, 109(2):367–384, Mar 2007.

[25] D Stamenović, J J Fredberg, N Wang, J P Butler, and D E Ingber. A microstructural approach to cytoskeletal mechanics based on tensegrity. *J. Theor. Biol.*, 181(2):125–136, July 1996.

[26] Gunnar Tibert and Sergio Pellegrino. *Deployable Tensegrity Masts*.

[27] Stephanie Wang and Albert Chern. Computing minimal surfaces with differential forms. *ACM Trans. Graph.*, 40(4):113:1–113:14, August 2021.

[28] Yafeng Wang and Xian Xu. Prestress design of tensegrity structures using semidefinite programming. *Advances in Civil Engineering*, 2019:5081463, Jan 2019.

[29] Qinglan Xia. Numerical simulation of optimal transport paths. In *2010 Second International Conference on Computer Modeling and Simulation*, volume 1, pages 521–525. IEEE, 2010.

[30] Junfeng Yang and Xiaoming Yuan. Linearized augmented lagrangian and alternating direction methods for nuclear norm minimization. *Mathematics of computation*, 82(281):301–329, 2013.